Chapter 10

Mesoscale Cellular Convection during Cold Air Outbreakes: A numerical study

A. Chlond[1] and G. Müller[2]

[1] *Max-Planck-Institut für Meteorologie, Hamburg, Germany*

[2] *Meteorologisches Institut, Universität Hamburg, Germany*

Abstract

A three-dimensional numerical model which makes use of a domain-doubling regridding technique is run to study the multi-scale eddy structure evolution during a cold-air outbreak. The simulations include the secondary-flow pattern transition starting with the relatively small-scale boundary layer rolls developing during the initial phase and ending with mesoscale cellular convection patterns. The model is applied to conditions of a cold-air outbreak observed during the ARKTIS 1991 experiment. It is demonstrated that the most important features of the observed situation are revealed by the model. Moreover, a sensitivity study is performed in order to investigate the relation between cell broadening and various physical processes. We found that latent heating due to condensation and cloud top radiative cooling are the most relevant processes leading to cell-broadening.

1 Introduction

The frequent occurrence of mesoscale cellular convection (MCC) patterns over vast regions of the oceans has been revealed by satellite imaging and its properties have been reviewed in detail by various authors (Agee et al., 1973; Agee, 1984). Areas of convective activity are usually associated with the flow of cold air over warm water, such as in cold air outbreakes (CAO) in midlatitudes. In such a case an initially cloud free and presumably stably stratified air mass is advected from land or an ice surface over a warmer sea surface. The heating and moistening from below causes the development of a convective boundary layer, in which a typical sequence of convection patterns whose geometric

properties change downstream could be observed: As soon as the cold air hits the warm sea, roll-like secondary flow patterns develop. Further downstream the roll patterns gradually change to cellular convection patterns, which can occur with either open or closed cells. Open cells consist of broad polygonal-shaped central areas of descending air, enclosed by relatively narrow rings of updraft, whereas closed cells are characterized by a reversed circulation direction.

Since cloud formation takes place almost only above areas of upward motion, these secondary flow patterns manifest themselves on satellite images. Cloud streets indicate the presence of roll vortices, whereas honeycomb-like cloud patterns are associated with cellular convection. An accumulation of observational evidence over the past 3 decades has allowed to identify the characteristics of rolls and cells during CAOs as well as the compilation of a climatology of MCC (Brown, 1980; Etling and Brown, 1993; Atkinson and Zhang, 1996) Near the coast or ice-edge, the rolls usually align along or at angles up to 15° from the mean horizontal wind of the convective layer, with lengths from 20 to 200 km, widths from 2 to 10 km and convective dephts from 1 to 2 km. Rolls occur in an environment of modest shear of horizontal wind (1 to 10 m s^{-1} km^{-1}). The typical value of aspect ratio ranges from 2 to 5. Both thermal and dynamic instabilities are regarded to play important roles in the generation of rolls. Downstream, the aspect ratios of the cellular patterns increase gradually up to the scale of MCC, reaching values of 10 to 30 for a distance of 500 to 1000 km from the shoreline. The cellular patterns have diameters ranging from 10 to 50 km and occur in a convective layer with a depth of about 1 to 3 km. Both the magnitude and the direction of horizontal wind in the convective layer change little with height. Cells occur in airstreams that are usually 2° to 5° C colder than the underlying sea surface. The total heat fluxes associated with cellular patterns range from 145 to 1200 W m^{-2}, the most frequent values being below 400 W m^{-2}.

The resemblance of atmospheric organized convection to the roll/hexagonal Rayleigh-Bénard convection patterns, observed in laboratory experiments and described by the classical linear theory developed by Lord Rayleigh (1916) suggests to regard MCC as an atmospheric analogue of the laboratory convection. However, according to Rayleigh-Bénard theory the most preferred aspect ratio of the cells is about 2.8 for a wide range of Rayleigh- and Prandtl-numbers, the primary determining parameters of the problem. This prediction, however, is inconsistent with the observational results mentioned above, which indicate that in CAOs cellular structures with varying aspect ratios up to 10 to 30 may be observed.

In order to explain the large discrepance in scale between atmospheric and classical Rayleigh-Bénard laboratory convection Rothermel and Agee (1986) showed, by numerically solving a nonlinear Boussinesq model, that a mesoscale organization of small-scale convective elements into a system with a collectively broad horizontal scale may be attributable to the nonlinearity inherent in the convection problem. Clark *et al.* (1986) used a two-dimensional nu-

merical model to examine the generation of gravity waves by two-dimensional rolls. They concluded that interaction between the rolls and the waves forces the rolls to choose a much increased horizontal spacing. In explanations for cell flattening of atmospheric convection many authors have appealed to the action of physical processes. Ray (1965) showed, using a linear model, that an anisotropy in eddy diffusion coefficients would increase the cell aspect ratio. However, Ray's calculations revealed that unrealistic large anisotropy ratios (horizontal component 200 to 400 times larger than the vertical component) would be required to produce typical cell flatness of MCC. Sasaky (1970) demonstrated that cell broadening may be due to the poor thermal conductivity of the upper boundary.

Using a two-dimensional nonlinear numerical model of convection, Sheu *et al.* (1980) investigated the effects of anisotropy of eddy diffusivity, large-scale subsidence and latent heat release upon cell flatness. They showed that each of the three physical factors tends to increase the aspect ratio. Brugge and Moncrieff (1985) simulated cellular convection with a two-dimensional numerical model. They concluded that radiative cooling at cloud top tends to produce closed-cell behavior. Sykes *et al.* (1988) used a two-dimensional numerical model to investigate the time-dependent development of cloud streets by numerically integrating the Boussinesq equations. They identified entrainment of buoyancy by the cloud as crucial for producing large aspect ratios by suppressing weaker upward-branches between the cloud streets. Fiedler and Peckham (1992) studied the conditions for generation of broad convection cells in a cloud-topped, convective, marine atmospheric boundary layer with an idealized two-dimensional model of non-precipitating moist convection. In their model broad cells appear when convective motions penetrate the inversion by a distance of at least half the average depth of the boundary layer, or when the rate of entrainment of dry air from above the inversion was substantially reduced. Three-dimensional numerical simulations of laminar, thermal convection between rigid boundaries with nearly constant heat flux, performed by Fiedler (1993), indicated that three dimensions were required for cell broadening.

Organized convection during CAOs is worthy of study for at least two reasons. First, the organization of convection on the mesoscale affects the net heating, drying, and horizontal momentum in the atmosphere. These features are of crucial importance for the general circulation and their effects should be included in cumulus parameterization schemes. Second, the theoretical understanding of organized convection is incomplete and, consequently, a gap exists in our understanding of the dynamics of the boundary layer. As discussed in the preceeding paragraph, the roles and interplay of different physical processes in the evolution of organized convection remain unclear. In particular, the basic problems of pattern transition and large aspect ratios remain unsolved. Three-dimensional models, with domains large enough to simulate the mesoscale structure in their larger contexts and with spatial resolutions fine enough to resolve the fine scale structure of rolls and cells, respectively, prob-

ably offer the best opportunity to attack these problems.

Here, the transition of convection patterns typically occurring during a CAO situation is investigated using a three-dimensional, nonlinear numerical model. Referring to a CAO observed during the ARKTIS 1991 experiment (Brümmer, 1992), leading to cloud-street development adjacent to an ice edge and ending with fully developed MCC 1000 km downstream, the boundary-layer development has been simulated. In addition, sensitivity runs have been performed in order to identify the physical processes that cause the transition of convection patterns. Since even state-of-the-art super-computers are overcharged in utilizing a numerical grid whose numerical mesh size enables the resolution of small-scale initial patterns and whose domain size is large enough in order to capture mesoscale convection patterns, the very large eddy simulation technique is applied with a spectral criterion for enlarging the domain: When the smallest resolvable scales contain insignificant energy then the horizontal resolution of the computational grid is adjusted to the scale of the dominant convective structures. This approach enables the simulation of convective patterns over the wide range of scales involved in the problem.

The paper is organized as follows. In section 2 we briefly describe the physical and numerical approach. Observations of a CAO and model results of the reference run are presented in section 3. In section 4 results of the sensitivity runs are dicussed to identify the most important factors promoting the broad length scales. Finally, summary and conclusions are given in section 5.

2 Very large eddy modelling

The model has been described in detail in Chlond (1992) and Müller and Chlond (1996). The general idea of the model is similar to that of a large eddy simulation model. The model explicitly calculates the spatial averages, which hopefully represent the dominant coherent large-scale motions, while parameterizing the effect of the small scales on the averaged flow quantities. The equations governing the resolved-scale motions are the three-dimensional, spatially averaged, incompressible Boussinesq equations conserving mass, momentum, liquid water potential temperature and total moisture content. The calculations are carried out in a Cartesian coordinate system that is translated with the geostrophic wind velocity to follow a trajectory of air starting near the ice edge. In that way, the CAO is treated as a time-dependent, quasi-local development.

The model includes most of the physical processes occuring in a moist boundary layer. It contains a water cycle (using a Kessler-type rain parameterization); it takes into account infrared radiative cooling in cloudy conditions (using an effective emissivity model) and the influence of large-scale vertical motions. The subgrid flux model is based on a transport equation for subgrid-

scale turbulent kinetic energy and is similar to that of Deardorff (1980) and Sykes et al. (1990). However, one should realize that the concept of subgrid modelling employed in LES-models could not entirely adopted here because the grid resolution in our model is too coarse and the scales resolved by the numerical grid do not fall within the inertial subrange. Therefore, in contrast to the LES modelling approach where the turbulent length scale is given by the average grid scale (see Chapter 3) we use a turbulent length scale that is proportional to the boundary layer depth. This approach has also been used by Sykes et al. (1988) and ensures that the parameterized fluxes contain the contributions of all three-dimensional motions not explicitely calculated by our resolved-scale model, independent of the resolution of the numerical grid.

The computational domain extends horizontally and vertically over a domain of size $L_x \cdot L_y \cdot L_z$. The vertical extension is $L_z = 5500$ m; L_x and L_y do not remain constant during the course of the integration and are specified below. The domain is split into $n_x = n_y = 64$ uniformly spaced horizontal intervals and $n_z = 50$ unequally spaced vertical intervals. To provide a good vertical resolution inside the boundary layer and especially near the inversion as the boundary layer grows, a simple regridding technique is used: A set of grids is generated that differ in that the zone where the finest resolution occurs varies with height. To calculate the tendencies we use a grid that provides the best resolution at the inversion height. In that way the zone of finest resolution moves with the inversion as it rises. The regridding of the model quantities of the old grid onto the new grid is carried out using linear interpolation. Logarithmic interpolation is used for the quantities defined at the grid points just above the surface. For details concerning the grid generation see Müller (1995). Cyclic lateral boundary conditions were applied and and a Rayleigh damping layer in the upper third of the domain was utilized to absorb vertically propagating gravity waves.

In order to study the flow pattern transition the horizontal resolution of the computational grid should be high enough (about 100 m) in order to resolve the relatively small-scale convection patterns developing during the initial phase of the event and, on the other hand, the horizontal size of such a model domain should cover about 100 km x 100 km in order to capture mesoscale cells. To run a three-dimensional model of such a type overcharges even state-of-the-art super-computers and therefore no 3-D simulation of a complete CAO has been performed until yet. In order to bypass the computer storage problem, the following strategy is applied for the 3-D simulation of the complete development: The simulation of the CAO is done using a grid box that is translated with the mean flow. During the initial phase, we use a domain size (6.4 km x 6.4 km) and a resolution (horizontal grid spacings 100 m) similar to that used by Sykes et al. (1990) and Chlond (1992). If the horizontal scales of the dominant convective structures show a tendency to grow, resulting in reduced energy levels of small-scale turbulent structures, the calculations are continued on a new grid with an unchanged number of grid points, but doubled horizontal domain size and grid spacings. The turbulent

flow patterns are translated from the old grid to the new one by horizontally completing the fields of the old grid in a periodic manner, taking advantage from the fact that periodic lateral boundary conditions are assumed. Since the number of grid points remains constant, the information of every second point of the old grid is lost due to the regridding procedure. If the cell broadening still continues during the course of integration, the domain will be enlarged in a corresponding manner and so on.

In our case, the domain was enlarged four times in order to simulate the boundary-layer development during a CAO. Hence, the horizontal size of the model domain increased from $L_x = L_y = 6.4$ km to $L_x = L_y = 12.8$, 25.6, 51.2 and 102.4 km, respectively, while the corresponding grid spacings increased from $\Delta x = \Delta y = 100$ m to $\Delta x = \Delta y = 200$, 400, 800 and 1600 m, respectively. The doubling of the horizontal mesh sizes results in a wavenumber cutoff. Therefore, the enlargement of the domain is only performed when the energy of the waves, which can not be resolved by the new grid, is smaller than a critical value. Here, a regridding is carried out, if less than 5% of the total energy content of the resolved turbulent structures could be attributed to those wavenumbers that cannot be resolved by the next grid. Hereby, the structure of the energy-spectrum of the turbulent patterns determines the moment at which a regridding is carried out. If the required condition is not fulfilled, no enlargement of the domain is performed. The spectrum of the resolved turbulent energy is analyzed during the course of integration by a two-dimensional Fourier analysis of the vertical-velocity field in a horizontal plan where the $\bar{w}$-variance has its maximum. This x-y-plane is typically located in the middle of the boundary layer or in the vicinity of the cloud base.

3 Simulation of a cold air outbreak

3.1 Observations and model input

In order to demonstrate the model's ability to reproduce the transition of convection patterns typically occurring during a CAO situation, we refer to a CAO observed on 8 March 1991 during the ARKTIS 1991 experiment. On this day between 10:30 and 12:30 UT, two research aircraft, a FALCON-20 and a DORNIER-128, flew horizontal and vertical soundings in order to detect the characteristics of a convective marine boundary layer developed under conditions of a CAO. Details on the experiment and the instrumentation are given in Brümmer (1992). The experimental area was located at the Norwegian Sea between Bear Island and Northern Norway and is marked on the NOAA-11 satellite image in Figure 1, which depicts the cloud situation at 12:49 UT on that day. The situation in the experimental area represents a late development phase of a CAO. An easterly flow caused cold air to flow off the ice pack

Fig. 1. NOAA-11 visible channel satellite image on 8 March 1991 at 12:49 UT. The white lines mark the flight patterns flown by the measure aircraft between 10:30 and 12:30 UT.

Table 1. Input parameters for the control run.

$\bar{\Theta}_l(z = z_T,\ t = 0) = 273$ K	$z_0 = 5 \cdot 10^{-4}$ m
$\Delta\bar{\Theta}_l(t = 0) = -11$ K	$z_T = 1 \cdot 10^{-4}$ m
$\Gamma_{\Theta_l} = 5.18 \cdot 10^{-3}$ K m^{-1}	$z_q = 1 \cdot 10^{-6}$ m
$\bar{q}(z = z_q,\ t = 0) = 3.7$ g kg^{-1}	$f = 1.387 \cdot 10^{-4}$ s^{-1}
$\Delta\bar{q}(t = 0) = -2.2$ g kg^{-1}	$u_g = 0$ m s^{-1}
$\Gamma_q = -2.73 \cdot 10^{-4}$ g kg^{-1} m^{-1}	$v_g = 22$ m s^{-1}
$F\downarrow(z_{TOP}) = 80$ W m^{-2}	
$\left(\frac{\partial\bar{\Theta}_l}{\partial t}\right)_{z=z_T} = 1.32 \cdot 10^{-4}$ K s^{-1}	$\left(\frac{\partial\bar{q}}{\partial t}\right)_{z=z_q} = \left(\frac{\partial\bar{q}}{\partial T}\right)^{SAT}\left(\frac{\partial\bar{\Theta}_l}{\partial t}\right)_{z=z_T}$

which encloses Novaya Zemlya. Here the air hit the relatively warm water of the Barents Sea heated by the easterly branch of the Gulf Stream. Before the air has reached the experimental area, it had been advected westward over a distance of about 1100 km. The heating from below caused the development of a convective boundary layer with cloud streets adjacent the ice edge. Further downstream, the rolls gradually changed to cellular convection. The boundary-layer depth was about 3 km and the aspect ratios defined by the cellular patterns range from 10 to 12.

To set up the control run we formulate the observed CAO-situation as an idealized problem: A geostrophic wind of 22 m s^{-1} blows out of 90^o (estimated by using the corresponding surface weather map). A north-south oriented straight shoreline separates an ice pack (eastward of the line) from the ocean with surface temperature varying normal to the shoreline, but uniform parallel to the shoreline. The model is driven by time-varying, but spatially uniform surface boundary conditions and an easterly geostrophic wind parallel to the y-axis. During the simulation, the computational domain, which first is located at the ice edge, is translated with the geostrophic wind. In case of growing horizontal scales of the dominant convective structures, the domain will be enlarged according to the procedure described in Section 2. One hour of integration time corresponds to a traveling distance of 79.2 km. Thus, the model domain has passed the experimental area after about 15 hours of integration time. The latitude has been taken to be 72^o N ($f = 1.387 \cdot 10^{-4}$ s^{-1}). At the shoreline a sea-surface temperature of 273 K at saturation ($\bar{q} = 3.7$ g kg^{-1}) is taken as lower boundary condition. Referring to the corresponding chart of the ice and sea surface temperature, published by the Norwegian Meteorological Institute, a temporal variation of $1.32 \cdot 10^{-4}$ Ks^{-1} in the sea surface temperature has been prescribed. This variation corresponds to a linear increase of about 6 K between the ice edge and the experimental area.

Different roughness lengths associated with momentum ($z_0 = 5 \cdot 10^{-4}$ m), heat ($z_T = 1 \cdot 10^{-4}$ m) and moisture ($z_q = 1 \cdot 10^{-6}$ m) have been employed. Following the concept of Sykes et al. (1990), we have adjusted these roughness lengths until the model-predicted surface fluxes were in reasonable agreement with aircraft data from ARKTIS 1991. Referring to the aircraft data, the downward infrared radiation flux impinging on the top of the model domain has been prescribed as $F \downarrow (z_{TOP}) = 80$ W m^{-2}.

Since no measurements are available at the ice edge, the initial profiles of temperature and humidity have been chosen in accordance with information taken from weather maps valid for the surface, the 850 hPa, the 700 hPa and the 500 hPa levels. Except for a superadiabatic surface layer, the initial atmosphere is prescribed as stably stratified with a lapse rate of $\Gamma_{\Theta_l} = 5.18 \cdot 10^{-3}$ Km^{-1}. The difference between the temperature at the sea surface and the first overlaying grid point at $z = z_1 = 15$ m has been chosen as $\Delta\bar{\Theta}_l = -11$ K, resulting in $\bar{\Theta}_l(z = z_1) = 262$ K. From saturation at the surface ($\bar{q} = 3.7$ g kg^{-1}) the initial moisture profile shows a strong drop ($\Delta\bar{q} = -2.2$ g kg^{-1}) to $\bar{q}(z = z_1) = 1.5$ g kg^{-1} at the first computational grid point. Above this point, $\bar{q}$ decreases linearly with a constant lapse rate ($\Gamma_q = -2.73 \cdot 10^{-4}$ g kg^{-1} m^{-1}). The initial wind profile is obtained by running a one-dimensional version of the model to a steady state, using the prescribed temperature and humidity profiles. The horizontally homogeneous solution is then transferred to the three-dimensional domain and perturbed by imposing small random perturbations on the temperature field at the first time step. The simulation of the boundary-layer development has been performed for a 15 h period. Table 1 summarizes the input parameters of the control run.

3.2 Model results

During the course of integration, the necessary condition permitting an enlargement of the model domain (as described in Section 2) was fulfilled after 0.5, 2, 4, and 9 h of integration time. The varying horizontal domain sizes and grid spacings used during different time intervals of the control run are listed in Table 2. Figure 2 shows the development of the boundary-layer height z_i, which also corresponds to the mean cloud top height, the cloud base height z_{cb}, and the stability parameter $-z_i/L$ (L denotes the Monin-Obukhov length) as a function of the shoreline distance y_d. First, the growth rate of z_i, which is largest near the ice edge, decreases downstream. Then, downstream of $y_d =$ 400 km, the growth rate remains almost constant on a relatively high level of about $\Delta z_i/\Delta y_d = 200$ m/100 km. This is due to the fact that the sea-surface temperature increases downstream by 0.6 K/100 km. Due to this continuously forcing, convection is maintained by positive surface fluxes of sensible and latent heat. At $y_d = 1050$ km, the distance between the shoreline and the center of the "U"-shaped experimental area seen in Figure 1, the simulation yields a

Table 2. Control run: Different horizontal sizes of computational domain (L_x, L_y) and grid spacings $(\Delta x, \Delta y)$ used for different integration time intervals (t) and corresponding ice-edge distances (y_d).

	$\Delta x, \Delta y$ [m]	L_x, L_y [km]	t [h]	y_d [km]
Grid 1	100	6.4	0 - 0.5	0 - 39.6
Grid 2	200	12.8	0.5 - 2	39.6 - 158.4
Grid 3	400	25.6	2 - 4	158.4 - 316.8
Grid 4	800	51.2	4 - 9	316.8 - 712.8
Grid 5	1600	102.4	9 - 15	712.8 - 1188.0

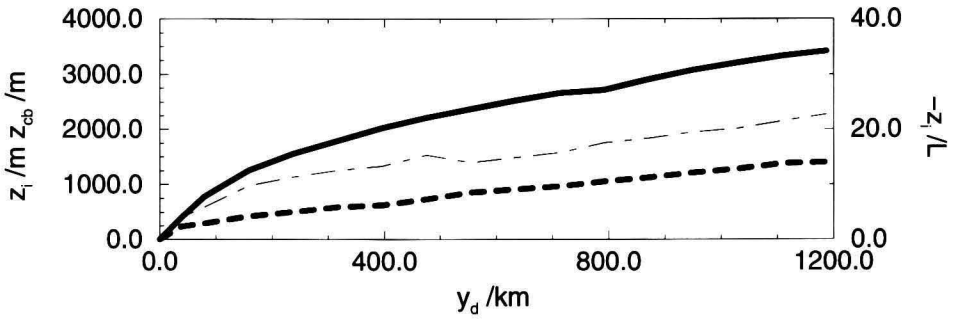

Fig. 2. Boundary-layer height z_i (full line, left ordinate), cloud base height z_{cb} (dashed line, left ordinate), and the stability parameter $-z_i/L$ (dashed-dotted line, right ordinate) versus shoreline distance y_d for the control run.

z_i-value of 3200 m, which roughly corresponds to the observed value of 3000 m. The cloud base height varies from $z_{cb} = 200$ m at $y_d = 40$ km to about $z_{cb} = 1280$ m at $y_d = 1050$ km resulting in a 1920 m deep cloud layer in the experimental area.

The stability parameter $-z_i/L$, also shown in Figure 2, rises from zero at the shoreline to about 20 at $y_d = 1050$ km. The parameter $-z_i/L$ has been used to relate the structure of convection to the stratification of the boundary layer. In our simulations rolls occur for $-z_i/L < 6$, corresponding to $y_d < 80$ km, while at greater distances from the shoreline cellular patterns dominate. These findings are roughly consistent with observations of Grossmann (1982) who found that for $-z_i/L < 7.3$ rolls dominate the convection structure, and that with increasing instability convective cells become important. However, recent observations of Hartmann et al. (1997) indicate that rolls could be the prevailing form of convection even for $-z_i/L$ arround 30, suggesting that $-z_i/L$ alone may be an inadequate indicator of conditions in which rolls are

supported.

The development of the resolved-scale eddies is illustrated in horizontal plan views of $\bar{w}$-fields shown in Figure 3. Each cross-section is taken from that vertical level where the $\bar{w}$-variance has its maximum. (These levels are localized near $z_i/2$ or in the vicinity of the cloud-layer base.) The contour plots are normalized by using the maximum values occurring in the different cross-sections.

The two cross-sections (a) and (b) at the upper panel of Figure 3 show the initial and the final state of the integration phase performed on the second grid ($L_x = L_y = 12.8$ km). The field seen in Figure 3a is the horizontally completed field which has developed on the first grid ($L_x = L_y = 6.4$ km). At $t = 0.5$ h, i.e. corresponding to a distance from the ice edge of about $y_d = 40$ km, the $\bar{w}$-field is organized in distinct bands indicating the presence of roll-shaped convection patterns. The rolls are oriented about 45^o to the left of the geostrophic wind i.e. about 28^o to the left of the surface wind and the maximum value of the $\bar{w}$-component is about 0.8 m s^{-1}. Figure 4 shows $\bar{w}$ power spectra, resulting from a two-dimensional Fourier analysis of the vertical-velocity fields, performed in x-y-planes which exhibit the largest $\bar{w}$-variance. Averaging of the Fourier-coefficients is performed in order to generate a one-dimensional presentation. At $t = 0.5$ h, the power spectrum peaks at horizontal wavelengths of 1.3 and 1.6 km. Since z_i amounts to 400 m, these wavelengths correspond to an aspect ratio ranging from 3 to 4.

While continuing the simulation on the second grid, the rolls change to cellular convection patterns. The convective activity increases resulting in a maximum (minimum) $\bar{w}$-value of about 4 m s^{-1} (-3 m s^{-1}) at $t = 2$ h ($y_d = 158$ km). These values are in agreement with observations (Melfi et al., 1985) and model results (Raasch, 1990) referring to similar conditions. The dominant horizontal wavelength as seen in Figure 3b has increased up to 3.2 km (see also Figure 4). Since z_i has grown faster than the dominant horizontal wavelength, the aspect ratio, A, has decreased towards 2.6. At this time, less than 5 % of total energy contained by the resolved turbulent eddies can be attributed to wavelengths which can not be resolved by the coarser grid with doubled horizontal mesh size. Thus, the condition permitting a regridding is fulfilled and the simulation is continued on the third grid with a horizontal domain size of $L_x = L_y = 25.6$ km. During this phase of integration, which ends at $t = 4$ h of total integration time ($y_d = 317$ km), convection keeps on being organized in cellular patterns and the dominant horizontal wavelength increases up to values of 6.4 to 8.5 km. In a layer of depth 1780 m A ranges now from 3.6 to 4.8.

Figure 3c,d depicts the initial and the final state of the next integration phase performed on the fourth grid ($L_x = L_y = 51.2$ km). During this phase, the turbulent structures keep on tending to select larger horizontal scales. At $t = 9$ h ($y_d = 713$ km), the condition for a new regridding is fulfilled. The aspect ratio A has increased up to 6.5, while the cloud-top height, z_i, is 2640 m. The maximum values of the $\bar{w}$-amplitudes are similar to those detected at

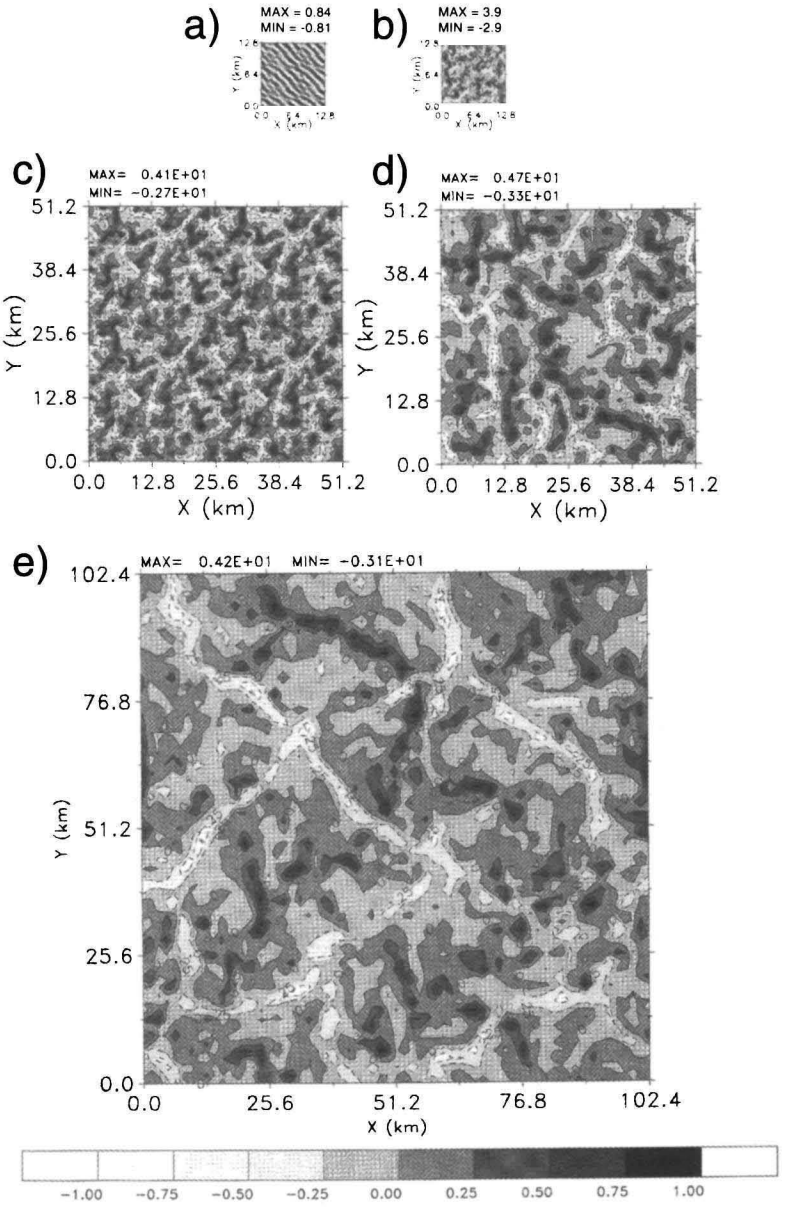

Fig. 3. Control run: Contour plots of the vertical velocity in horizontal x-y cross-sections of differently sized computational domains used for the control run. Each cross-section is located at the vertical level with largest $\bar{w}$-variance. Shown is the situation (a) at time $t = 0.5$ h (corresponding distance from ice edge $y_d = 39.6$ km) at level $z = 520$ m (grid 2); (b) at $t = 2$ h, ($y_d = 158.4$ km, $z = 601$ m, grid 2); (c) at $t = 4$ h ($y_d = 316.8$ km, $z = 938$ m, grid 4); (d) at $t = 9$ h, ($y_d = 712.8$ km, $z = 1445$ m, grid 4); (e) at $t = 15$ h, ($y_d = 1188.0$ km, $z = 1799$ m, grid 5). The vertical velocity is normalized by using the maximum occurring in the cross-section (maximum indicated).

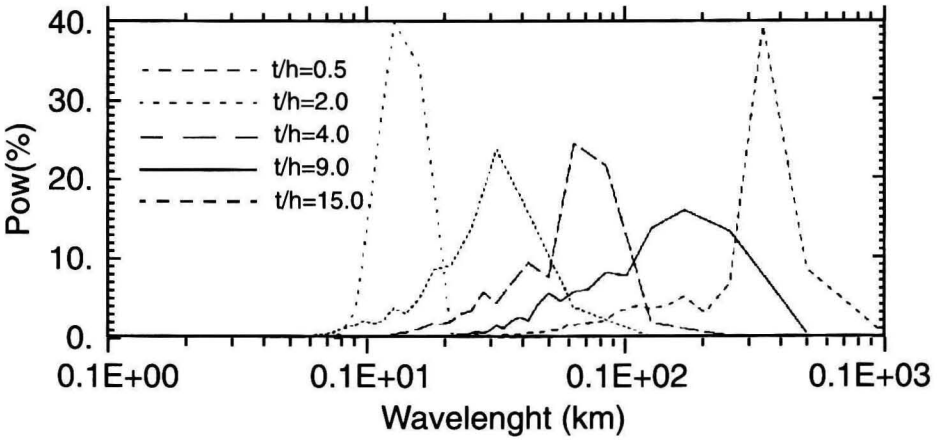

Fig. 4. Control run: Vertical velocity power spectra resulting from two-dimensional Fourier analyses of x-y cross-sections located at the vertical levels with largest $\bar{w}$-variances. An averaging of the Fourier coefficients is performed in order to generate a one-dimensional presentation. Shown is the percentage of total energy as a function of the horizontal wavelength λ at $t = 0.5$ h ($z = 520$ m), $t = 2$ h ($z = 601$ m), $t = 4$ h ($z = 876$ m), $t = 9$ h ($z = 1530$ m) and $t = 15$ h ($z = 1760$ m) with $Pow(\lambda) \equiv \frac{\text{energy}(\lambda)\cdot 100}{\text{total energy}}$.

$t = 2$ h.

Figure 3e shows the final situation at $t = 15$ h ($y_d = 1188$ km) on the fifth grid ($L_x = L_y = 102.4$ km). At this time, the condition permitting the next regridding is not fulfilled. (The contribution of those eddies, which are not resolvable on the next grid, to the total energy is about 10 %.) The corresponding $\bar{w}$ power spectrum (Figure 4) indicates that the vertical velocity field is dominated by a horizontal wavelength of 34.1 km, while z_i has grown up to 3390 m. Thus, A has grown up to 10, the scale of MCC. This value is in agreement with the aspect ratio (10 to 12) observed in the experimental area. The maximum values of the $\bar{w}$-amplitudes (about 4m s^{-1} and -3 m s^{-1}, respectively) have not changed significantly during the phase of cellular convection.

Figure 5 shows isopleths of the normalized $\bar{q}_l$-field for a vertical x-z cross-section of the fifth model domain at $t = 15$ h (left panel) and the corresponding horizontal x-y plan view of the liquid water path (LWP)-field (right panel), defined by the vertical integral of $\rho\bar{q}_l$, i.e. LWP=$\int \rho\bar{q}_l \mathrm{d}z$. The vertical x-z cross-section is located along the line $y = L_y/2 = 51.2$ km of the model domain. The mean cloud base and cloud-top height are located at 1600 m and 3400 m, respectively. There is a variation in cloud-top heights of about 200 m and in cloud-base heights of about 500 m. The maximum liquid water content has reached 0.9 g kg^{-1}. As seen in the horizontal plan view, the $\bar{q}_l$-field does not exhibit a horizontal homogeneous structure, but shows a clear positive correlation with the corresponding $\bar{w}$-field (given in Figure 3e): Large values

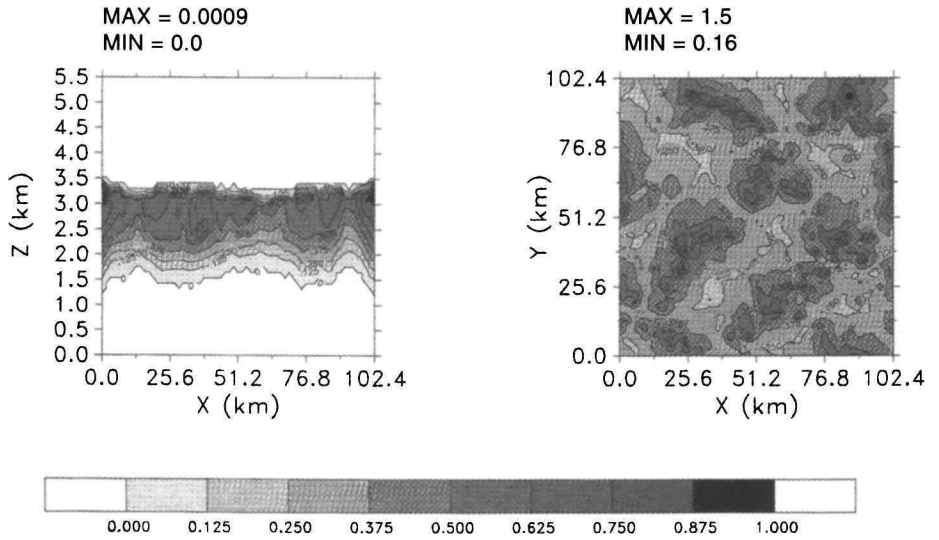

Fig. 5. Isopleths of the normalized $\bar{q}_l$-field for a vertical x-z cross-section located at $y = L_y/2 = 51.2$ km of the model domain (left panel) and a horizontal x-y plan view of the liquid water path, (right panel) at $t = 15$ h ($y_d = 1188$ km) for the control run.

of $\bar{q}_l$ occur simultaneously with strong ascending motions while descending motions are related to small $\bar{q}_l$-values. At $t = 15$ h, mesoscale cellular patterns, marked by large values of liquid water content, are discernible. These patterns are similar to those observed in cases of MCC. Admittedly, these patterns don't look like ideal open cells which should have a cloud free area surrounded by a narrow ring of clouds. The simulated cells rather exhibt features of mixed cells as they incorporate characteristics of open as well as of closed cells. Nevertheless, we think that despite the fact that the cloud cover estimated by the model did not match the observations in detail and that the simulated liquid water content appears too large at the cell centers, we think that the three-dimensional model did a fairly good job at reproducing the overall characteristics of open MCC.

4 Towards the understanding of cell broadening

Sensitivity tests were performed in order to examine the sensitivity of cell broadening, occurring in case of a CAO situation, with respect to various physical processes. The control case was re-run with following modifications:

- Experiment 1 [no $\bar{q}_l$]: Liquid-water formation due to condensation is artificially turned off.

- Experiment 2 [no lat. h.]: With cloud formation, but latent heating due to condensation and evaporation is artificially turned off.
- Experiment 3 [no rad.]: Long-wave radiation is turned off.
- Experiment 4 [rad.+]: Long-wave radiative cooling occurring at cloud top is enhanced by prescribing a downward infrared radiation flux impinging on the top of the model domain as $F\downarrow(z_{TOP}) = 10$ W m^{-2} (instead of $F\downarrow(z_{TOP}) = 80$ W m^{-2}).

Table 3. Dominant aspect ratios and sizes of model domains at $t = 15$ h for the control run and the sensitivity runs.

Run	$A(\bar{w})$ [ ]	$A(LWP)$ [ ]	L_x, L_y [km]
Control run	10.1	10.1	102.4
Exp. 1 [no $\bar{q}_l$]	2.7	–	51.2
Exp. 2 [no lat. h.]	8.6; 5.7	8.6	102.4
Exp. 3 [no rad.]	5.4; 4.1; 2.7	5.4	51.2
Exp. 4 [rad.+]	14.7	14.7	102.4

Figure 6 shows $\bar{w}$ power spectra, resulting at $t = 15$ h from a two-dimensional Fourier analysis of the vertical-velocity fields performed in x-y-planes which exhibit the largest $\bar{w}$-variances for the control run and the sensitivity runs. As in case of Figure 4 , averaging of the Fourier coefficients is performed in order to generate a one-dimensional presentation. Shown is the percentage of total energy as a function of the aspect ratios, which are calculated from the respective z_i-values and the horizontal wavelengths. The dominant aspect ratios for the control run and the sensitivity runs, $A(\bar{w})$, defined at $t = 15$ h by the $\bar{w}$-fields are listed in Table 3. Additionally, we list the dominant aspect ratios resulting from the analyses of the power spectra of the LWP-fields, $A(LWP)$. If the power spectra exhibit more than one peak, the corresponding aspect ratios are listed according to their energy content, i.e. the first number corresponds to the aspect ratio related to the energy peak of largest magnitude, the second number corresponds to the aspect ratio related to the energy peak of secondary magnitude and so on. Since not all runs ended on the fifth grid, the horizontal dimension L_x, L_y of the model domain used at $t = 15$ h is also indicated.

4.1 Experiment 1: No formation of liquid water

The increase of the aspect ratio up to the scale of MCC does not occur in case when we have suppressed liquid water formation. At $t = 15$ h, A has only grown up to 2.7. This value corresponds to the aspect ratios observed in case

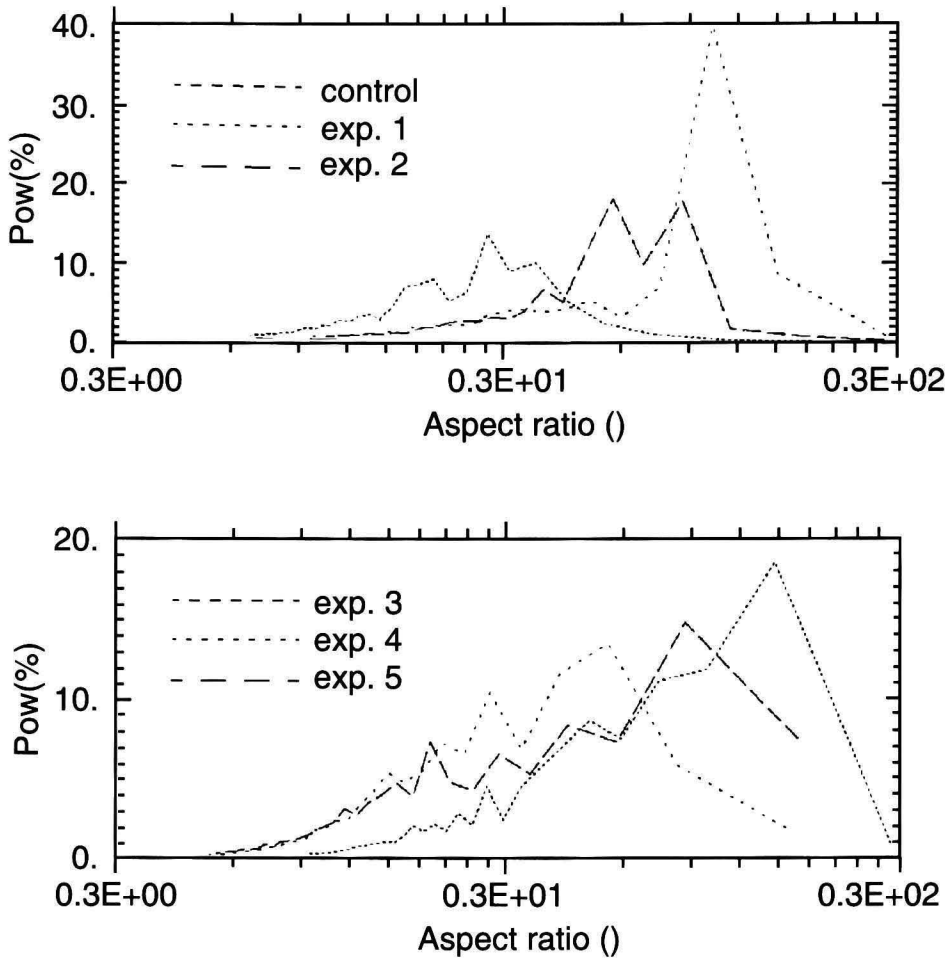

Fig. 6. Vertical velocity power spectra at levels with largest $\bar{w}$-variances at $t = 15$ h for the control run and the sensitivity runs. An averaging of the Fourier coefficients has been performed in order to generate a one-dimensional presentation. Shown is the percentage of total energy as a function of the aspect ratio A with $Pow(A) \equiv \frac{\text{energy}(A)\cdot 100}{\text{total energy}}$.

of the Rayleigh-Bénard convection. It also agrees with aspect ratios detected in cloudless convective boundary layers (clear-air-turbulence), typically ranging from 1 to 4 (Hardy and Ottersten, 1969). The condition permitting the application of the fifth grid has not been fulfilled and the run ends on the fourth grid with $L_x = L_y = 51.2$ km.

As a consequence of the artificial cutoff of the condensation process, no formation of precipitation, no latent-heat release and no long-wave radiative cooling can occur. Compared to the control run, some characteristics of the boundary-layer are modified: The cloud-top height is reduced from 3400 m to 2340 m, the temperature jump defining the capping inversion is reduced from

5 K to 2.7 K (which should have an impact on entrainment processes) and the mean boundary-layer temperature (273.5 K for the control run) is reduced by 1.1 K (which results in an increase of the surface flux of sensible heat). Thus, a problem to interpret results of non-linear models becomes evident: Since all physical processes affect each other by non-linear interactions, the artificial tuning or excluding of one process changes the effect of various other processes. In our case, it is not possible to decide whether the small-scale convective structure is due to (a) the suppression of the one process taken into consideration, (b) the indirect modification of an other process or (c) the interaction of two or more modified processes. This fact has to be taken into consideration whenever the results of sensitivity studies performed with a non-linear model are interpreted.

4.2 Experiment 2: No latent heat release

Excluding latent heat release results in moderately reduced aspect ratios. At $t = 15$ h the $\bar{w}$ power spectrum exhibits two peaks of almost the same magnitude at wavelengths defining aspect ratios of 8.6 and 5.7. The $\bar{q}_l$-field is dominated by only one wavelength, giving $A = 8.6$. Although latent heating is excluded, $\bar{q}_l$-formation is allowed to take place. Thus, the clouds are treated as "dry clouds" or "dust clouds" that can be influenced by long-wave radiative processes. As in the control run, a closed cloud deck has developed. Hence, the infrared radiative cooling impacts the convective structures in a similar manner than in the control run. Formation of precipitation takes place, but does not affect the thermodynamics.

The fact that a larger aspect ratio of the convective cells can be found in the control run suggests that latent heating tends to increase the aspect ratio. Some other features of the boundary layer which have been modified with respect to the control run also may affect the aspect ratio. These are: z_i is reduced by 400 m, the temperature jump at the capping inversion has increased from 5 K in the control run up to 6.5 K (possibly leading to a modification of entrainment processes) and the mean boundary-layer temperature has decreased by 2 K (leading to an increased surface flux of sensible heat). Modifications in q do not affect physical processes since q is treated like a passive tracer with respect to the thermodynamics. In contrast to the present case, the experiment 1 leads to a decrease of the temperature jump at the capping inversion. Since experiment 1 as well as experiment 2 result in reduced aspect ratios, the strength of the capping inversion does not seem to have a crucial impact on the aspect ratios.

Concerning the thermodynamics, the differences between experiments 1 and 2 are only due to long-wave radiation processes. Experiment 1 results in a smaller dominant aspect ratio than the present run does. This gives reason to conclude that the long-wave radiative cooling tends to increase the aspect

ratio.

4.3 Experiment 3: No long-wave radiation processes

The exclusion of radiation processes reduces the aspect ratios significantly. The $\bar{w}$-field is dominated by an aspect ratio of $A = 5.4$, 4.1 and 2.7 (the energy content of the corresponding wavelengths decreases from left to right). The cloud field is dominated by a single wavelength giving $A = 5.4$. The differences between the dominant wavelengths resulting from the $\bar{w}$- and the LWP-spectra are due to the fact that not all branches of upward motion reach the upper level of the boundary layer. Thus, not all upward branches are associated with cloud formation. The run ends on the fourth grid with $L_x = L_y = 51.2$ km. The comparison with the control run again suggests, that long-wave cloud-top cooling enlarges the aspect ratio.

4.4 Experiment 4: Increased radiative cloud-top cooling

The reduced downward infrared radiation flux impinging on the top of the model domain as $F \downarrow (z_{TOP}) = 10$ W m^{-2} (instead of $F \downarrow (z_{TOP}) = 80$ W m^{-2}) results in almost a doubling of the long-wave radiative cloud-top cooling. At $t = 15$ h, the maximum of the horizontally averaged cooling rate amounts to 4.7 K h^{-1} (instead of 2.5 K h^{-1} for the control run). The enhanced radiative cloud-top cooling enlarges the the dominant aspect ratios of the $\bar{w}$- and the $\bar{q}_l$-field significantly up to 14.7 (instead of 10 for the control run).

The boundary-layer features are relatively similar to those of the control run. The main differences are: the temperature jump at the capping inversion increased by 1.5 K, the mean boundary-layer temperature decreased by 1 K, z_i increased by 100 m and the total amount of precipitation formed during the course of integration decreased by about 12 %. The liquid water path is almost identical to that of the control run. Thus, the amount of latent heat release do not differ much in both cases. Since the indirect modifications of other processes are relatively small, we conclude, that the increase of the aspect ratio is the result of the increased cloud-top cooling.

Compared to the control run, the maximum amplitudes of negative $\bar{\Theta}_v$-fluctuations occurring at the bottom of the boundary layer increased by about 25 %. (In case of experiment 3, the corresponding amplitudes decreased by about 30 %). This indicates that the radiative cloud-top cooling tends to produce colder downdrafts.

To explain the well broadening due to radiative cooling we propose the following conceptual mechanism. Convective downdrafts reaching the surface cause a divergent, horizontal flow adjacent to the sea surface. The heating

from below tends to increase the temperature of the horizontally moving air and as soon as the air becomes warmer than the surrounding air, i.e. when the air has become sufficiently buoyant, it moves upward and forms an updraft. As a consequence, an increased temperature difference between the cold downdraft and the surrounding air at the lower part of the boundary layer requires more heating from below in order to generate an updraft. In order to increase the heating, the horizontally moving air has to be in contact with the warm sea surface for a longer time, i.e. it has to pass an elongated horizontal distance (when the velocity of convective motions remains unchanged). As a result, the cooling of downdrafts increases the aspect ratio because it increases the horizontal distance which has to be passed by the horizontally outflowing downdraft-air before the air becomes positively buoyant. This concept is appropriate to explain the cell-broadening effect of cloud-top cooling and the validity of this concept is also supported by modelling efforts reported by Fiedler (1993). He performed three-dimensional numerical simulations of laminar, thermal convection between rigid boundaries with nearly constant heat flux and showed that cell broadening is the result of the poorly conducting boundaries.

5 Summary and conclusions

Referring to a CAO, observed during the ARKTIS 1991 experiment and leading to cloud-street development adjacent to an ice edge and ending with fully developed MCC, the boundary-layer development has been simulated by using a three-dimensional, nonlinear numerical model. A regridding technique was introduced, which enables the simulation of turbulent motions with growing horizontal scales. The simulation starts on a high-resolving grid which covers a relatively small-sized computational domain. When the horizontal scales of the dominant convective structures have grown to a certain degree, the flow patterns are transferred by horizontal completion to a new grid with doubled horizontal domain size and grid spacings. The regridding is performed, when the energy of the eddies unresolvable by the coarser grid decreased below a critical value. By repeating this procedure four times, the convection-pattern transition occurring during a CAO has been simulated.

Compared to the observations, the model tends to overpredict the cloud-cover, but the most important characteristics typically observed during a CAO-event are revealed by the model: (1) The depth of the boundary layer first grows rapidly as the cold air flows off the ice over relatively warm water. Further downstream, the rate of boundary-layer grow decreases. 1000 km downstream, the cloud-top height agrees with the observations. (2) Roll-like secondary-flow patterns, appearing adjacent to the ice edge, change downstream to cellular flow patterns whose dominant aspect ratio increases down-

stream up to 10. This value agrees fairly well with the aspect ratio observed in the experimental area. (3) Upward (downward) motions are correlated with large (small) liquid-water concentrations. Thus, convection patterns defined by the vertical-velocity field are also reflected by the cloud field.

Sensitivity studies have been performed in order to investigate the relation between cell broadening and various physical processes. Latent heating due to condensation and especially radiative cloud-top cooling have been identified as processes leading to cell-broadening. The artificial cutoff of liquid-water formation prevents the enlargement of convective scales.

We have proposed a conceptual model, which elucidates the mechanism by which cloud-top cooling may generate larger aspect ratios. This concept requires an enhanced temperature-difference between cold downdrafts and the surrounding air of the lower boundary layer in order to generate enlarged aspect ratios. However, the temperature of the downdrafts is not only affected by cloud-top cooling: formation of precipitation and entrainment of warmer and drier air from the inversion may increase the temperature of the downdrafts. Evaporative cloud-top cooling, occurring when entrained air mixes up with cloudy boundary-layer air, may decrease the downdraft-temperature. An additional complication results from the fact that all these processes affect each other by nonlinear interactions. This may be the reason for the striking high variability of results, yielded by numerous investigators who have tested the convective-scaling effect of different physical processes and external meteorological conditions.

Finally, as a kind of outlook, we would like to make a few comments concerning the parameterization issue. Since it has now become apparent that rolls and cells are an ubiquitous phenomenon durning CAOs their effects should be represented in a larger scale context. General circulation models and even global numerical weather-prediction models with a typical grid size of less than 100 km cannot resolve individual convective cells and their accompanying mesoscale circulations. These are subgrid-scale processes, whose collective effects on the larger-scale fields must somehow be determined or parameterized. Cloud resolving models (CRMs) such as LES- and VLES-models are potentially very powerful tools to address this issue because of their ability to supply much more extensive information about the physics involved than can be obtained from costly and time-consuming observational campaigns of actual convective events. The idea is that CRMs can contribute to understanding of the physical processes which control the heat, moisture and momentum fluxes that determine the thermal and dynamical structure of the boundary layer. Moreover, CRMs can generate a database which could be used to test closure assumptions and to calibrate closure coefficients to improve existing parameterization schemes or to develop new ones. However, the use of CRMs to develop parameterizations, either using statistical techniques or through improved physical understanding, will require CRMs to be validated using data obtained from a wide variety of different observational case studies, as well as to verify model results by intercomparison studies. Only if this is succesful

we can apply with confidence the knowledge gained from the CRM simulations to the development of more realistic parameterizations for weather- and climate-prediction models.

Acknowledgement

The authors wish to thank Prof. Dr. B. Brümmer for his useful comments and close interest in this study. The research reported here was funded by the Deutsche Forschungsgemeinschaft under SFB-318 grant.